

Local nonlinear tidal bar dynamics

Abstract

The long-term dynamics of tidal bars in a confined tidal channel is studied by a new numerical model of intermediate complexity. The simplicity of the model allows a comparison of its results with those obtained from a linear stability analysis of a flat bottom. The aim of this chapter is to study the sensitivity of the tidal bar evolution and possible equilibria to channel width and the Coriolis parameter. For this a configuration that crudely mimics the Exe estuary is chosen. The model simulates tidal bars that extend beyond the middle axis of the channel, as is also observed in nature and in a laboratory. The simulations suggest that while the Coriolis effect strongly alters the initial growth of tidal bars, its impact on the equilibrium patterns is smaller. In one simulation (in which the channel is twice as wide as in the default setting) the bars seem to have reached a morphodynamic equilibrium after approximately a century, but changed to a drastically different pattern after approximately two and a half centuries. The pattern after a century was strongly influenced by the Coriolis effect, however, the pattern after 2.5 centuries was not. This highlights the problem of studying the long-term evolution using time integrations: it is unclear when and if a pattern corresponds to a morphodynamic equilibrium. To overcome this problem, equilibrium patterns and their stability are analysed by means of Newton's method. This results in morphodynamic equilibria for different channel widths. For increasing widths, the bars extend further over the channel axes and the maximum bottom height of the patterns moves away from the channel boundary.

5.1 Introduction

In the preceding chapters, only the initial formation of tidal bars was studied. In that stage of their formation the heights of the bars are assumed to be small compared to the water depth. To gain insight in the evolution of bars after this initial stage, various approaches can be taken. One such approach employs high-complexity numerical models. In this approach, typically an entire channel from the sea (an open boundary) up to the landward boundary (closed or river) is considered. Usually, an initially sloping bottom topography is imposed and a tidal wave enters the channel from the open boundary. This approach is followed in, for example, Hibma et al. (2003, 2004), van der Wegen and Roelvink (2008), Tambroni et al. (2010), Xie et al. (2017) and Olabarrieta et al. (2018). However, the complexity of such models hinders a detailed analysis of the dynamics that are responsible for the observed bottom patterns and their sensitivity to model parameters.

The models described in the paragraph above are global models. So-called local models can be employed, typically in an idealized setting, when aiming at gaining a more fundamental understanding about the dynamics of tidal bars. In these models, only a short section of a long channel, with a constant width and depth is considered. The water motion in this domain is driven by a spatially uniform pressure gradient and periodic boundary conditions are imposed. This allows one to study the formation of tidal bars without considering the effects of the open and closed boundaries or the morphodynamic adjustment of the sloping bottom topography. Such local models were successful in unraveling the physical mechanism of the initial growth of tidal bars (Seminara and Tubino, 2001, Schramkowski et al., 2002, see also Chapters 3 and 4).

When tidal bars mature, their heights are no longer small compared to the water depth and their dynamics become nonlinear. Nonlinear dynamics can result in complex phenomena, such as multiple equilibria, limit cycles (i.e., bottom patterns that evolve periodically in time) and/or chaos. Schramkowski et al. (2004) investigated whether such phenomena occur in the dynamics of tidal bars. In contrast to most studies on nonlinear bars, they did this by using a local, mathematically tractable model in which the governing equations were projected on Fourier modes. Next, they considered the possible morphodynamic equilibria and their stability properties by performing a bifurcation analysis in two bifurcation parameters, the bottom friction coefficient and the channel width. The starting point of this analysis was the trivial morphodynamic equilibria that describes a uniform tide over a flat horizontal bottom. They found that, depending on the channel width, the flat bottom equilibrium becomes linearly unstable through a critical or subcritical pitchfork bifurcation when increasing the friction parameter beyond a critical value. The manifestation of a subcritical bifurcation implies the existence of multiple equilibria. Further increasing the friction parameter resulted in a Hopf bifurcation that

leads to time periodic solutions. However, their model approach was limited to weak friction; it turned out that for (realistically) large friction parameter values, too many (and unclear which) Fourier modes were needed. This made the continuation to realistic values of bottom friction computationally unfeasible.

In this chapter, we build a numerical local model, which is not limited to weak bottom friction. This model allows us to explore the long-term evolution and, if existent, nontrivial morphodynamic equilibria that represent tidal bars, where the search for morphodynamic equilibria is restricted to steady states. The study of Schramkowski et al. (2004) motivates the first question that we aim to answer in this chapter: 1) In the new model, do nontrivial tidal bar equilibria exist in the parameter regime with realistic values of the friction parameter? The second question concerns the sensitivity of the long-term dynamics to model parameters. Field observations of Dalrymple and Rhodes (1995) and Leuven et al. (2016) suggest that the channel width is an important parameter for the tidal bar dynamics. This finding is also observed in the available local models and complex numerical models (see earlier citations). Moreover, numerical studies (Xie et al., 2017, Olabarrieta et al., 2018) and the results of Chapter 4 show that there are physically relevant parameter regimes (for moderate to small values of the Rossby number) where the Coriolis force significantly affects the initial growth of the spatial patterns of tidal bars. This motivates the second question: 2) How does the long-term evolution and possibly equilibria patterns depend on channel width and the Coriolis parameter? Lastly, in the linear stability analyses of Seminara and Tubino (2001) and Schramkowski et al. (2002) (see also Chapters 3 and 4) the fastest growing bottom perturbation of a flat bottom was studied, because this pattern dominates the spatial structure of the pattern that initially forms. This raises the third question: 3) To what extend do bottom patterns on the long-term resemble the fastest growing patterns found with the linear stability analysis of the flat bottom?

This chapter is organized as follows. In Section 5.2, the model and the numerical implementation is described. This section is followed by a description of the numerical experiments and their results. It starts with verifying that the model reproduces results of Chapter 3. Subsequently, the output of four time integration simulations of the long-term evolution with different channel width and latitude values is presented. The results of the time integration runs are followed by the (preliminary) results obtained using a numerical continuation approach. Here, the sensitivity of the morphodynamic equilibria to channel width is systematically investigated. In Section 5.4, a comparison of the model results with observed tidal bars is discussed together with the extent to which the long-term evolution and possibly equilibria patterns resemble the fastest growing patterns found with the linear stability analysis of the flat bottom. Section 5.4 ends with discussing limitations of the model and it is followed by the conclusions in Section 5.5.

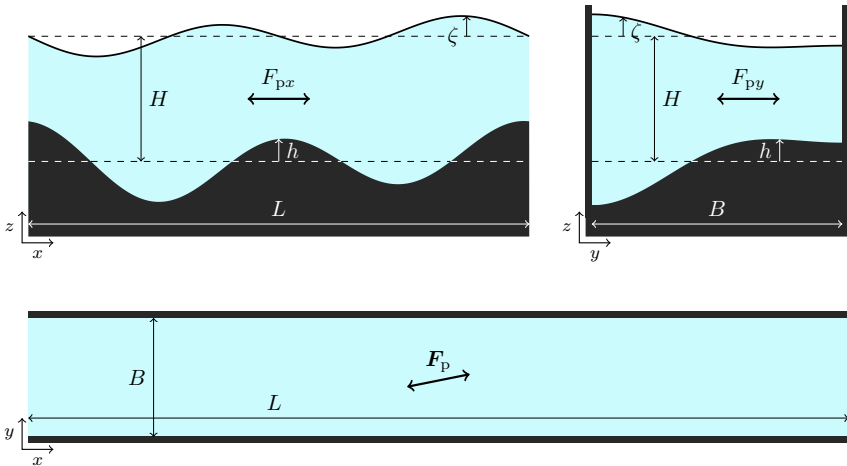


Figure 5.1: Model domain viewed from an along-channel cross-section (top-left panel), a lateral cross-section (top-right panel) and from the top (bottom panel). Here, x , y and z are the along-channel, lateral and vertical coordinate, L denotes the length, B the width and H the undisturbed channel depth. The bottom height is denoted by h , the sea surface elevation by ζ . Lastly, $\mathbf{F}_p = (F_{px}, F_{py})$ denotes the imposed tidal pressure gradient force.

5.2 Methods

5.2.1 Model

The local numerical morphodynamic model is based on the *Morfo55* model, described in Yuan et al. (2016) (originally developed by Caballeria et al., 2002, Garnier et al., 2006). Here, we present a new model, adopted from the *Morfo55* model, to study the dynamics of bottom patterns in a section of a confined tidal channel. Because the original *Morfo55* model was designed to study bottom patterns at the coast or on the continental shelf (in a periodic domain), a second closed boundary condition had to be added to allow for a channel geometry. Furthermore, other formulations for sediment transport are added for consistency with the previous two chapters.

The model domain consists of a short section of a long channel. The section has length L , width B and undisturbed water depth H (see Figure 5.1). The domain length is assumed to be short compared to the tidal wavelength and the length scale on which the channel width varies. Moreover, the shallow water approximation is used, the tidal amplitude is assumed to be small compared to the undisturbed depth and the bottom is assumed to evolve on a timescale much longer than the tidal period. Finally, the sediment is assumed to be uniform and the water motion is forced by an imposed spatially uniform tidal

pressure gradient force.

Let $\mathbf{x} = (x, y)$ denote the spatial coordinate, with x the along-channel coordinate and y the lateral coordinate of the domain $[0, L] \times [0, B]$ and let t denote the time coordinate. The evolution of the bottom height $h(t, \mathbf{x})$, with respect to the mean bed level $z = -H$, is governed by

$$\frac{\partial h}{\partial t} = -\frac{1}{1-p} \nabla \cdot (\mathbf{q}_b + \mathbf{q}_s). \quad (5.2.1)$$

Here, $\nabla = (\partial/\partial x, \partial/\partial y)$, p is the porosity parameter and $\langle \cdot \rangle$ denotes the average over one tidal period $2\pi/\sigma$ with σ the principal frequency of the imposed tidal pressure gradient force \mathbf{F}_p . The right-hand side of the bottom evolution equation (5.2.1) contains the tidally-averaged convergence of the bedload sediment transport $\mathbf{q}_b = (q_{bx}, q_{by})$ and the suspended load sediment transport $\mathbf{q}_s = (q_{sx}, q_{sy})$.

The formulation of the bedload sediment transport is based on the formulation from Bagnold (1963) with a bed slope term adopted from Bailard (1981), and reads

$$\mathbf{q}_b = \alpha_b \mathcal{H}(u_e^2 - u_c^2)(u_e^2 - u_c^2) (\mathbf{u} - \Lambda u_e \nabla h), \quad (5.2.2)$$

where α_b is a bed load constant, \mathcal{H} the Heaviside function (which is one when its argument is positive and zero otherwise), u_c the critical velocity for erosion and Λ is a bed slope constant. Furthermore, u_e is the effective velocity given by (Roos et al., 2004),

$$u_e^2 = \|\mathbf{u}\|^2 + \frac{1}{2} \left(\frac{u_w H}{H + \zeta - h} \right)^2,$$

with $\mathbf{u}(t, \mathbf{x}) = (u, v)$ the depth-averaged current velocity, u_w the near-bed wave orbital velocity amplitude (taken constant here) and $\zeta(t, \mathbf{x})$ the free surface elevation induced by the bottom perturbations. The second term crudely accounts for the effect of wave stirring on sediment transport.

The suspended load sediment transport and concentration is calculated following (the appendix of) ter Brake and Schuttelaars (2010). The suspended load transport reads

$$\mathbf{q}_s = \mathbf{u} C - \mu (\nabla C + c_b \nabla h + c_t \nabla \zeta). \quad (5.2.3)$$

Here, $C(t, \mathbf{x})$ is the depth-integrated volumetric sediment concentration. The last three terms in equation (5.2.3) represent horizontal diffusion of sediment and result from assuming an approximate balance between the vertical turbulent mixing and downward settling which fixes the vertical distribution of sediment concentration. Furthermore, μ is the horizontal eddy diffusivity (taken constant here) and c_b and c_t are the sediment concentration at the surface and at the bottom, respectively. The latter two are given by

$$c_b = \frac{w_s C}{\kappa_v} \left(1 - e^{-\frac{w_s}{\kappa_v}(H+\zeta-h)} \right)^{-1} \quad \text{and} \quad c_t = \frac{w_s C}{\kappa_v} \left(e^{\frac{w_s}{\kappa_v}(H+\zeta-h)} - 1 \right)^{-1},$$

with w_s the settling speed and κ_v the vertical eddy diffusivity (also taken constant). The concentration C is calculated using an advection-diffusion equation,

$$\frac{\partial C}{\partial t} + \nabla \cdot \mathbf{q}_s = \alpha_s \mathcal{H}(u_e^2 - u_c^2)(u_e^2 - u_c^2) - w_s c_b, \quad (5.2.4)$$

where the first term on the right hand side models the erosion of sediment from the bed, with α_s an erosion parameter. The second term models the deposition of suspended sediment.

To obtain the sediment transport, the tidal current \mathbf{u} and sea surface elevation ζ are needed. These are calculated by solving the depth-averaged shallow water equations, which consist of the continuity and momentum equations,

$$\frac{\partial \zeta}{\partial t} + \nabla \cdot ((H + \zeta - h)\mathbf{u}) = 0, \quad (5.2.5)$$

$$\frac{\partial \mathbf{u}}{\partial t} + (\mathbf{u} \cdot \nabla)\mathbf{u} + \frac{c_d \|\mathbf{u}\| \mathbf{u}}{H + \zeta - h} + g \nabla \zeta + f \mathbf{E} \mathbf{u} = \mathbf{F}_p. \quad (5.2.6)$$

Here, c_d is a drag coefficient, g the gravitational acceleration, $\mathbf{F}_p(t) = (F_{px}, F_{py})$ an externally prescribed pressure gradient force that drives the tidal flow and $f = 2\Omega \sin(\varphi)$ the Coriolis parameter, where Ω the rotation rate of the Earth and φ the latitude (both taken as constant within the domain). The matrix \mathbf{E} reads

$$\mathbf{E} = \begin{pmatrix} 0 & -1 \\ 1 & 0 \end{pmatrix}.$$

Following Yuan et al. (2016), the external pressure gradient force per unit mass is given by

$$\mathbf{F}_p = \frac{\partial \mathbf{u}_0}{\partial t} + \frac{c_d \|\mathbf{u}_0\| \mathbf{u}_0}{H} + f \mathbf{E} \mathbf{u}_0, \quad (5.2.7)$$

with $\mathbf{u}_0 = (U \sin(\sigma t), 0)$ the current with amplitude U and frequency σ induced by the external pressure gradient in the absence of bottom patterns. That is, \mathbf{F}_p is chosen such that when $h = 0$ the current $\mathbf{u}(t, \mathbf{x}) = \mathbf{u}_0(t)$.

To solve the system of equations (5.2.1)–(5.2.6), periodic boundary conditions are imposed in the along-channel direction with period L for all variables h , ζ , \mathbf{u} and C . Furthermore, there is no transport of water and sediment through the channel walls, resulting in the lateral boundary conditions

$$v = 0 \quad \text{and} \quad q_{sy} = q_{by} = 0 \quad \text{at} \quad y = 0, B.$$

5.2.2 Numerical implementation

While *Morfo55* was implemented in Fortran, the current model is implemented in the Julia programming language (Bezanson et al., 2017). As a result, compared to the Fortran code, the model is easier to read, less prone to errors and it integrates well with existing scientific computing Julia software. Following the

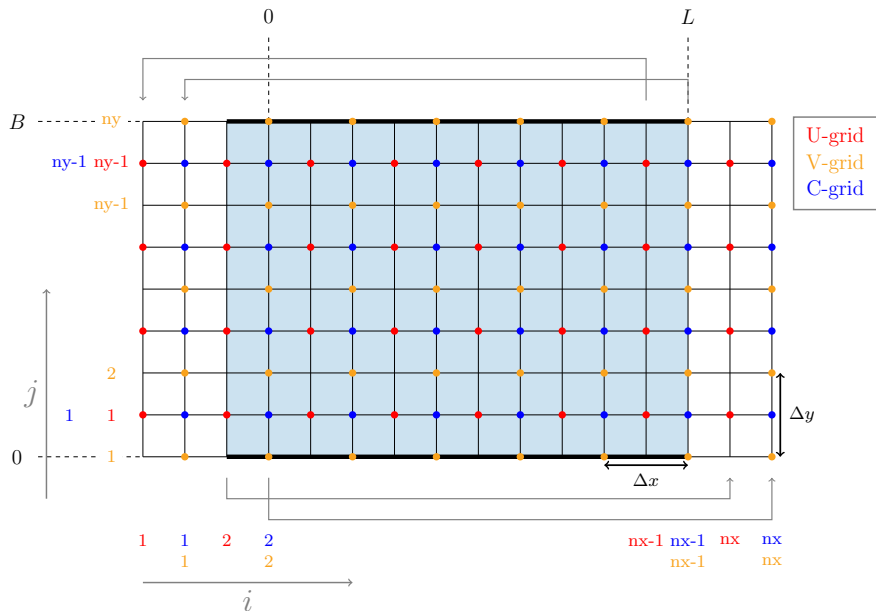


Figure 5.2: Top view of the discretized model domain. The shaded blue area denotes the physical domain. The points outside the shaded area are the ghost points to implement the periodic boundary condition. To that end, the values at the end and beginning of the physical domain are copied to the ghost points (represented by the gray arrows).

Morfo55 model, the equations are discretized in space by second-order finite difference methods on a regular, rectangular staggered Arakawa C-grid with resolution Δx by Δy in the along-channel and lateral direction, respectively. This grid consists of three subgrids, the U -, V - and C -grid, which are shifted with respect to each other (see Figure 5.2). The along-channel current u and the sediment transports q_{sx} and q_{bx} , are calculated at the U -grid. The lateral current v and sediment transports q_{sy} and q_{by} are calculated at the V -grid. The concentration C , the free surface elevation ζ and the bottom height h are calculated at the C -grid. The U - and C -grid have $N = (n_x - 2)(n_y - 1)$ grid points in the physical domain (denoted with shaded blue in the figure), while the V -grid contains $N_v = (n_x - 2)n_y$ grid points.

Apart from the grid points in the physical domain, so-called ghost points are defined. These ghost points are used to implement the periodic boundary conditions (in the x -direction). That is, the values at (x_2, y_j) are copied to (x_{n_x}, y_j) for all j , as well as the values at (x_{nx-1}, y_j) to (x_1, y_j) (depicted in Figure 5.2 by the gray arrows). The lateral boundaries are imposed at the V -grid (i.e., the grid where the lateral velocity v and the lateral sediment transports q_{sy} and q_{by} are calculated) by requiring: $v = 0$, $q_{sy} = 0$ and $q_{by} = 0$.

In the bed evolution equation (5.2.1) the convergence of sediment transport is averaged over one tidal cycle (see Chapter 3 or 4 for a discussion). This separates the long morphodynamical timescale from the short hydrodynamical timescale and allows us to calculate the convergence of sediment transport during one tidal cycle in which the bottom height is held fixed. Let $\Psi_h(t)$ be a $(3N + N_v)$ -dimensional vector consisting of the free surface elevation ζ , along-channel current velocity u , lateral velocity v and the suspended sediment concentration C at time t at every grid point (x_i, y_j) in the physical domain. The subscript of Ψ_h refers to an N -dimensional vector h containing the bottom height h at every grid point (x_i, y_j) in the physical domain. It denotes that Ψ_h is calculated given fixed values of the elements of h . The discretized hydrodynamic equations (5.2.5)–(5.2.6) and the concentration equation (5.2.4), read

$$\frac{\partial \Psi_h}{\partial t} = g_h(\Psi_h), \quad (5.2.8)$$

with $g_h : \mathbb{R}^{3N + N_v} \rightarrow \mathbb{R}^{3N + N_v}$ a nonlinear function, where the subscript again denotes the fixed values of the bottom height. Solving equation (5.2.8) can be thought of as writing ζ , u and C in terms of h , which allows us to write the the full system of discretized equations as one system of ordinary differential equations (ODEs),

$$\frac{\partial h}{\partial t} = f(h), \quad (5.2.9)$$

with $f : \mathbb{R}^N \rightarrow \mathbb{R}^N$ a nonlinear function representing the convergence of tidally averaged sediment transport at every grid point.

5.2.3 Time integration

To solve $\Psi_h(t)$ for a fixed bottom height \mathbf{h} , the ODEs in (5.2.8) are integrated over one tidal cycle with the Runge-Kutta 4 method (RK4) with fixed time steps of Δt (Shampine, 2005, Rackauckas and Nie, 2017). Knowing $\Psi_h(t)$ over a complete tidal cycle allows the calculation of the convergence of the tidally averaged sediment transport $\nabla \cdot (\mathbf{q}_s + \mathbf{q}_b)$, resulting in $\mathbf{f}(\mathbf{h})$. After a certain number of spin-up cycles of equation (5.2.8) (for realistic values of model parameters, this is typically 2), equation (5.2.9) is subsequently integrated in time by the Euler Forward method with time steps of $\Delta\tau$.

5.2.4 Continuation

To systematically investigate the dependency of morphodynamic equilibria and their stability to model parameters, such as channel width and latitude, a predictor-corrector continuation technique is used (e.g., Kuznetsov, 2004). Given a parameter setting P and a morphodynamic equilibrium \mathbf{h} , the predictor predicts a new equilibrium \mathbf{h}' for the parameter setting P' in which the parameters are slightly changed. That is, it transforms the equilibrium \mathbf{h} , of parameter setting P to a pattern \mathbf{h}' for which $\mathbf{f}(P', \mathbf{h})$ is close to zero. The corrector, in turn, corrects this pattern such that it is in fact an equilibrium and satisfies

$$\mathbf{f}(P', \mathbf{h}') = 0. \quad (5.2.10)$$

Using the continuation methodology, equation (5.2.9) is replaced by equation (5.2.10). Hence, only the time integration of equation (5.2.8) is still necessary. When the channel width is varied, not only a parameter, but also the grid changes. The predictor in that case consists of stretching or squeezing the previous solution by Δy , followed by an interpolation onto the numerical C -grid. The corrector step is done with the Newton method implemented in BifurcationKit.jl (Veltz, 2020).

The boundary conditions are such that the total amount of sediment is not allowed to change. When using Newton's method, this restriction is not necessarily satisfied. Moreover, the phase of the bottom pattern is not uniquely determined: if $h(x, y)$ is an equilibrium, also $h(x + c, y)$, with c a constant real number, will result in a zero right hand side of equation (5.2.1) since the problem is translational invariant. The nonuniqueness of solutions to equation (5.2.10) hinders the Newton method. To remedy this, \mathbf{f} is adapted in two ways. Denote the adapted \mathbf{f} with a tilde: $\tilde{\mathbf{f}}$. The i -th component of \mathbf{h} , \mathbf{f} and $\tilde{\mathbf{f}}$ are denoted by \mathbf{h}_i , \mathbf{f}_i and $\tilde{\mathbf{f}}_i$, respectively for $i = 1, \dots, N$. For $i = 2, \dots, N - 1$, the components of \mathbf{f} and $\tilde{\mathbf{f}}$ are the same, $\mathbf{f}_i = \tilde{\mathbf{f}}_i$. The first adaptation of \mathbf{f} is that its first component is replaced by a Dirichlet condition that determines the phase of the pattern: $\mathbf{f}_1(\mathbf{h}) = \mathbf{h}_1$. This results in equilibria where $\mathbf{h}_1 = h(0, 0) = 0$. The second adaptation assures mass conservation

by imposing a zero mean bottom height: $\tilde{\mathbf{f}}_N(\mathbf{h}) = \sum_i \mathbf{h}_i$. That is, the last equation in (5.2.10) is replaced by an integral condition.

To find equilibria with the Newton method, the Jacobian matrix of $\tilde{\mathbf{f}}$ is needed. This matrix, evaluated at a bottom pattern \mathbf{h} , reads

$$\tilde{\mathbf{J}}(\mathbf{h}) = \begin{pmatrix} \frac{\partial \tilde{\mathbf{f}}_1}{\partial \mathbf{h}_1}(\mathbf{h}) & \cdots & \frac{\partial \tilde{\mathbf{f}}_1}{\partial \mathbf{h}_N}(\mathbf{h}) \\ \vdots & \ddots & \vdots \\ \frac{\partial \tilde{\mathbf{f}}_N}{\partial \mathbf{h}_1}(\mathbf{h}) & \cdots & \frac{\partial \tilde{\mathbf{f}}_N}{\partial \mathbf{h}_N}(\mathbf{h}) \end{pmatrix}.$$

Since $\tilde{\mathbf{f}}$ contains a time integral, calculating $\tilde{\mathbf{J}}$ by hand is complicated. Options to calculate the Jacobian are the use of symbolic software or by employing finite differences (Dijkstra et al., 2014). Here, we opt for the (forward) automatic differentiation method (see e.g., Griewank and Walther, 2008). This boils down to using the chain rule consistently and smart bookkeeping. The idea is to save both the result and the derivative after every elementary operation of the code that calculates $\tilde{\mathbf{f}}(\mathbf{h})$ (e.g., addition, multiplication, etc.). When $\tilde{\mathbf{f}}$ is differentiable at \mathbf{h} , this results in the calculation of the Jacobian matrix $\tilde{\mathbf{J}}(\mathbf{h})$ without making truncation errors. The automatic differentiation is done with the ForwardDiff.jl package (Revels et al., 2016).

The stability of an equilibrium \mathbf{h} follows from the spectral decomposition of the Jacobian matrix $\mathbf{J}(\mathbf{h})$ (no tilde). This matrix is calculated in the same way as $\tilde{\mathbf{J}}(\mathbf{h})$ but by taking the derivative of \mathbf{f} rather than $\tilde{\mathbf{f}}$. That is, without the integral and Dirichlet condition. The eigenvalue problem to be solved reads

$$\mathbf{J}(\mathbf{h})\mathbf{v} = \omega\mathbf{v}, \quad (5.2.11)$$

with $\mathbf{v} \neq 0$ the normalized eigenvectors and ω the corresponding eigenvalues. The eigenvalues are sorted by their real part: $\text{Re}\{\omega_1\} \geq \dots \geq \text{Re}\{\omega_N\}$. If the real part of ω_1 is negative, the equilibrium \mathbf{h} is linearly stable. The corresponding eigenvector \mathbf{v}_1 is in the direction in which perturbations of the equilibrium dampens the slowest. On the other hand, when there are eigenvalues with positive real part, the equilibrium is linearly unstable. The eigenvector \mathbf{v}_1 , corresponding to the eigenvalue with the largest real part ω_1 , points in the direction in which perturbations grow the fastest.

For $\tilde{\mathbf{f}}$ and \mathbf{f} to be differentiable with respect to \mathbf{h} , two modifications to the governing equations are made. The first is that the Heaviside function \mathcal{H} in equation (5.2.4) and (5.2.2) is replaced by a hyperbolic tangent in the continuation code,

$$\mathcal{H}(u_e^2 - u_c^2) \approx \frac{1 + \tanh(\delta_1(u_e^2 - u_c^2))}{2},$$

where $\delta_1 = 10 \text{ s}^2 \text{ m}^{-2}$ tunes the steepness of the smoothed jump. The second is that $\|\mathbf{u}\|$ in the quadratic friction term is replaced by $(u^2 + v^2 + \delta_2)^{1/2}$ with $\delta_2 = 10^{-5} \text{ m}^2 \text{ s}^{-2}$. These two modifications are only made for the continuation runs, because especially the first is computationally expensive.

5.2.5 Analysis of model output

In Section 5.3, the results are analysed by calculating the root-mean square height at time t , which is a measure of the kinetic energy of the bottom pattern and defined as

$$h_{\text{rms}}(t) = \frac{\|\mathbf{h}(t)\|}{\sqrt{N}} \approx \left(\frac{1}{LB} \int_0^L \int_0^B h(t, x, y)^2 \, dx \, dy \right)^{1/2},$$

where $\|\cdot\|$ denotes the Euclidean norm. Moreover, the patterns are analysed with respect to an appropriate Fourier basis. That is, the bottom height at time t is written as

$$h(t, x, y) = \sum_{m,n=-\infty}^{\infty} h_{m,n}(t) e^{2\pi i \left(\frac{n}{2B}y + \frac{m}{L}x\right)},$$

with $h_{m,n}$ a complex number for every integer m and n . This allows one to analyse the time evolution of the different Fourier coefficients $h_{m,n}$ in both the initial formation and the long-term evolution of the bottom patterns.

5.2.6 Design of experiments

In Section 5.3, three types of model experiments will be performed. The setup of each type is discussed below. We base the channel characteristics on those of the Exe estuary in England. That is, the channel is of the order of 3 m deep, about 1 km wide and the tidal currents are in the order of 0.5 m s^{-1} . A complete description of the default parameter values is listed in Table 5.1. The sections below contain the differences from the default setting for each type of experiment.

Verification

We verify that the model reproduces results of Chapter 3 in three different manners. First, the growth rates calculated in Chapter 3 are compared with the eigenvalues of the Jacobian matrix $\mathbf{J}(0)$. Second, the eigenvectors of this Jacobian are compared with the eigenfunctions in Chapter 3. The former are supposed to be finite dimensional (i.e., discretized) representations of the latter. Third, the morphodynamic time integration is tested by projecting the bottom height resulting from a time integration run onto the eigenvector of the Jacobian $\mathbf{J}(0)$ with the largest growth rate. The time series of the amplitude of this pattern is compared with the time series of the exponential growth of the corresponding eigenvalue. The morphodynamic time integration is initialized with a random bottom perturbations between -10 and 10 cm (with mean zero and satisfying the boundary conditions).

Parameter	Value	Unit	Description
B	1	km	channel width
H	3	m	undisturbed channel depth
L	10	km	domain length
Δy	50	m	lateral grid space
Δx	100	m	longitudinal grid space
Δt	5	s	hydrodynamical time step
$\Delta\tau$	1	week	morphological time step
U	0.5	m s^{-1}	background current amplitude
σ	$2\pi/44700$	s^{-1}	M_2 tidal frequency
g	9.81	m s^{-2}	gravitational acceleration
c_d	0.0025		drag coefficient
Ω	$7.29 \cdot 10^{-5}$	s^{-1}	angular speed of Earth rotation
φ	50	$^\circ \text{N}$	latitude
u_c	0.3	m s^{-1}	critical erosion velocity
w_s	0.013	m s^{-1}	settling velocity
μ	10	$\text{m}^2 \text{s}^{-1}$	horizontal eddy diffusivity
κ_v	0.01	$\text{m}^2 \text{s}^{-1}$	vertical eddy diffusivity
α_s	$5 \cdot 10^{-6}$	s m^{-1}	erosion suspended sediment parameter
α_b	$3 \cdot 10^{-4}$	s m^{-1}	bedload parameter
u_w	0.25	m s^{-1}	near-bed wave orbital velocity amplitude
Λ	2		bed slope parameter
p	0.4		porosity

Table 5.1: Model parameters. Their values are based on the Exe estuary (see Chapter 3 and references therein). The value of the near-bed wave orbital velocity amplitude u_w is the same as in Yuan et al. (2016) and Roos et al. (2004).

To compare the model output of the nonlinear model with that of the linear model of Chapter 3, a number of simplifications are made to the current model. First of all, the Coriolis effect is neglected, the quadratic bottom shear stress replaced by a linear one,

$$\frac{c_d \|\mathbf{u}\| \mathbf{u}}{H + \zeta - h} \rightarrow \frac{8c_d U \mathbf{u}}{3\pi(H + \zeta - h)}$$

and only the bed slope (diffusive) part in the bedload transport is considered:

$$\mathbf{q}_b = -\alpha_b \Lambda \|\mathbf{u}\|^3 \nabla h.$$

Furthermore, the last term in the suspended sediment transport (5.2.3) is neglected, $c_t = 0$, and in the expression for c_b , the depth $H + \zeta - h$ is replaced by the constant undisturbed channel depth H . Moreover, the critical current velocity for sediment movement and the near-bed wave orbital velocity are set to zero, $u_c = 0$ and $u_w = 0$, the channel depth is $H = 5$ m, the background current velocity amplitude is $U = 1$ m s⁻¹, the eddy diffusivity $\mu = 1$ m² s⁻¹ and the latitude $\varphi = 0^\circ$. Note that a difference between the two model formulations remains, namely the sea surface elevation ζ induced by the bottom topography.

Time integration

To compare the fastest growing patterns obtained from the linear stability analysis with the long-term evolution and to study the (transient) long-term evolution of tidal bars for different values of the channel width B and the Coriolis parameter, four time integration runs are performed. The channel width is chosen to be equal to $B = 1$ km or $B = 2$ km and the latitude $\varphi = 0^\circ$ or $\varphi = 50^\circ$ N. The bottom height is again initialized with random values between -10 and 10 cm with mean zero and satisfying the boundary conditions. In contrast to the verification experiments, the full model is used, with parameter values as in Table 5.1. The length L of the domain is 10 km. This value is chosen such that multiple bars in the along-channel direction can form. However, its choice remains somewhat arbitrary and the sensitivity of the model results to this choice will be discussed in Section 5.4.

Continuation

To systematically investigate the effect of channel width on the spatial pattern of the morphodynamic equilibria, a numerical continuation is performed. To speed up the calculations, a slightly simplified model setting is used for this: $u_c = 0$, $u_w = 0$, $\varphi = 0^\circ$, $c_t = 0$ and the depth $H - h + \zeta$ in c_b is replaced by the undisturbed depth H . The stability of the equilibria is calculated using the Jacobian matrix $\tilde{\mathbf{J}}$, which was calculated during the Newton iteration. That

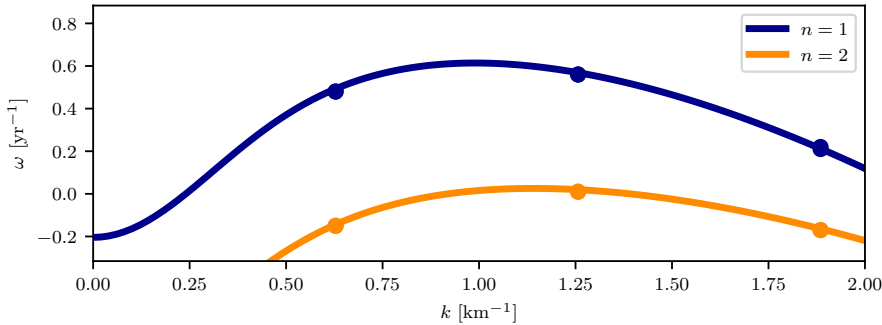


Figure 5.3: Growth rate of perturbations of the trivial equilibrium $h = 0$ versus along-channel wavenumber k . The different colors denote different lateral mode numbers. The solid lines are calculated with the model in Chapter 3. The colored dots are the eigenvalues of the Jacobian $\mathbf{J}(0)$ at the trivial equilibrium $\mathbf{h} = 0$ calculated by the model described in this chapter. The parameters values are as in Table 5.1 with $U = 1$ m/s, $H = 5$ m, $u_c = 0$, $u_w = 0$, $\mu = 1$ m 2 s $^{-1}$, $\varphi = 0^\circ$, $c_t = 0$, the depth $H - h + \zeta$ in c_b is replaced by the undisturbed depth H , the bottom stress is linear in \mathbf{u} and the only the bed slope part in the bedload transport is considered.

is, instead of computing \mathbf{J} and solving the eigenvalue problem (5.2.11), the stability is determined by solving the generalized eigenvalue problem $\tilde{\mathbf{J}}(\mathbf{h})\mathbf{v} = \omega \mathbf{M}\mathbf{v}$, where $\mathbf{M} = \text{diag}(0, 1, \dots, 1, 0)$ is a singular diagonal matrix with zeros at the first and last element of the diagonal and ones elsewhere. In the future this could be redone by using \mathbf{J} , as described in Section 5.2.4.

5.3 Results

5.3.1 Verification

Using the the model setting discussed in Section 5.2.6, the eigenvalues of the Jacobian are plotted in Figure 5.3, together with the growth rates calculated with the model discussed in Chapter 3 for various along-channel wavenumbers k . The figure shows that the correspondence is good. Since the Coriolis effect is neglected, the eigenvectors of $\mathbf{J}(0)$ are discretized versions of

$$\cos(k(x - \phi)) \cos\left(\frac{n\pi}{B}y\right),$$

with k and ϕ real numbers and n an integer (see Chapter 3). In Figure 5.4 the eigenvectors obtained with the numerical model are plotted. Figure 5.4 shows that that the patterns can be associated with a real number k and integer n . Moreover, the presence of two independent eigenvectors per eigenvalue, show that the patterns are translational invariant and that the value of ϕ is

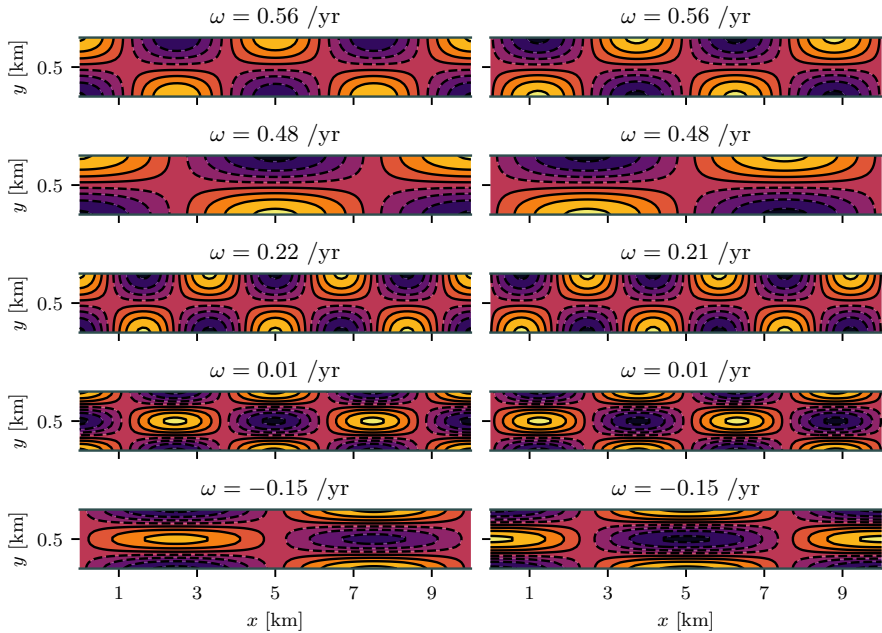


Figure 5.4: Contour-color plots of eigenvectors of the Jacobian $\mathbf{J}(0)$ at the trivial equilibrium $\mathbf{h} = 0$ corresponding to the largest (in real part) eigenvalues for lateral mode number $n = 1$ and $n = 2$. The parameters values are as in Table 5.1 with $U = 1$ m/s, $H = 5$ m, $u_c = 0$, $u_w = 0$, $\mu = 1$ m 2 s $^{-1}$, $\varphi = 0^\circ$, $c_t = 0$, the depth $H - h + \zeta$ in c_b is replaced by the undisturbed depth H , the bottom stress is linear in \mathbf{u} and the only the bed slope part in the bedload transport is considered.

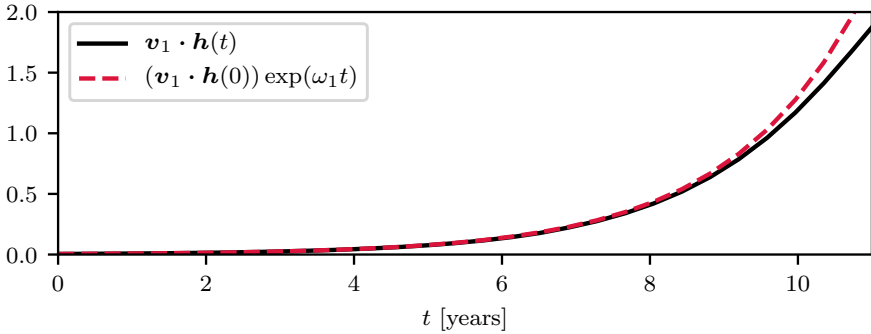


Figure 5.5: The solid black line is the bottom height $\mathbf{h}(t)$ projected onto the first eigenvector \mathbf{v}_1 versus time t : $\mathbf{v}_1 \cdot \mathbf{h}(t)$ (i.e., the amplitude of the fastest growing bottom pattern versus time). The dashed red line shows the exponential function $(\mathbf{v}_1 \cdot \mathbf{h}(0))e^{\omega_1 t}$ (red dashed line), where ω_1 is the eigenvalue corresponding to \mathbf{v}_1 . The parameters values are as in Table 5.1 with $U = 1 \text{ m/s}$, $H = 5 \text{ m}$, $u_c = 0$, $u_w = 0$, $\mu = 1 \text{ m}^2 \text{s}^{-1}$, $\varphi = 0^\circ$, $c_t = 0$, the depth $H - h + \zeta$ in c_b is replaced by the undisturbed depth H , the bottom stress is linear in \mathbf{u} and the only the bed slope part in the bedload transport is considered.

arbitrary. To test the morphodynamic time integration, the flat bottom profile is perturbed with random disturbances and integrated in time. The solid black line in Figure 5.5 shows the time evolution of the bottom height vector $\mathbf{h}(t)$, projected onto the first eigenvector (top left panel in Figure 5.4). This evolution compares well with the exponential growth of the eigenvector corresponding to the largest eigenvalue of the Jacobian (dashed red line).

5.3.2 Time integration

Figure 5.6 shows the time evolution of the root-mean square height of the four simulations described in Section 5.2.6. In the first two simulations, indicated by the solid black and red lines in the figure, the channel width B is 1 km, while in the third and fourth simulations, indicated by the blue and cyan line, the channel is 2 km wide. In the first and third simulation the Coriolis parameter is zero (i.e., latitude $\varphi = 0^\circ$), whereas in the second and fourth simulation the latitude is $\varphi = 50^\circ \text{ N}$. After an initial growth, the root-mean square height of the pattern becomes approximately constant in time. This period is longer for the wider channels. The root-mean square height of patterns after 1000 years in the wider channels are larger than those in the narrow channels. Moreover, in the 1 km wide channels the root-mean square height after 1000 years is slightly larger if the Coriolis effect is included compared to the case where it is not, while the opposite holds for the 2 km wide channels.

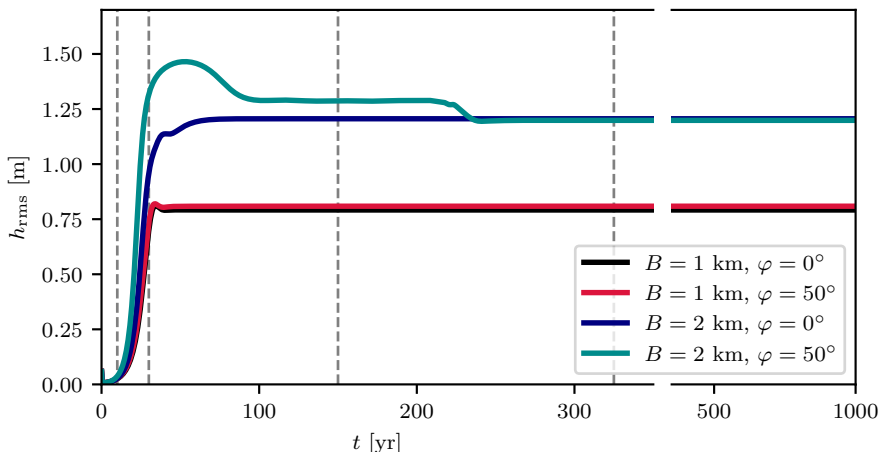


Figure 5.6: Root-mean square height h_{rms} versus time t for four different simulations. The vertical lines denote the moments in time at which the patterns are shown in Figures 5.7–5.10. Parameter values used are as in Table 5.1.

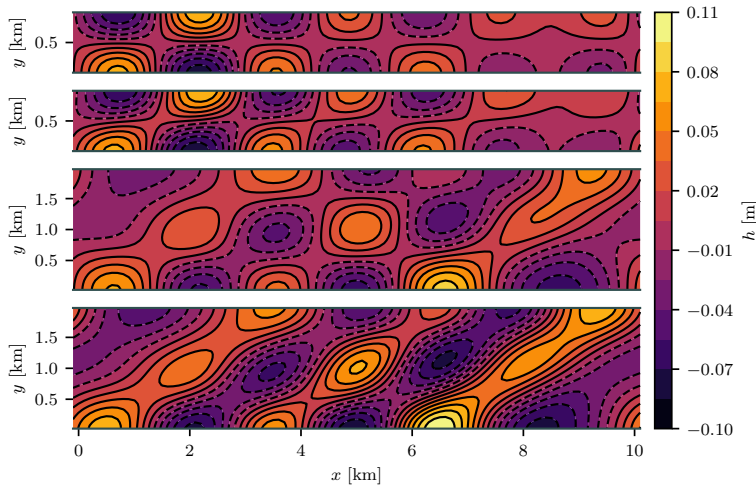


Figure 5.7: Bottom height versus space after $t = 10$ years for four different simulations. In the top two panels the channel width $B = 1$ km and in the bottom two the channel width is $B = 2$ km. In the first and third panel the latitude $\varphi = 0^\circ$, while in the second and bottom panel the latitude $\varphi = 50^\circ$. Parameters values used are as in Table 5.1.

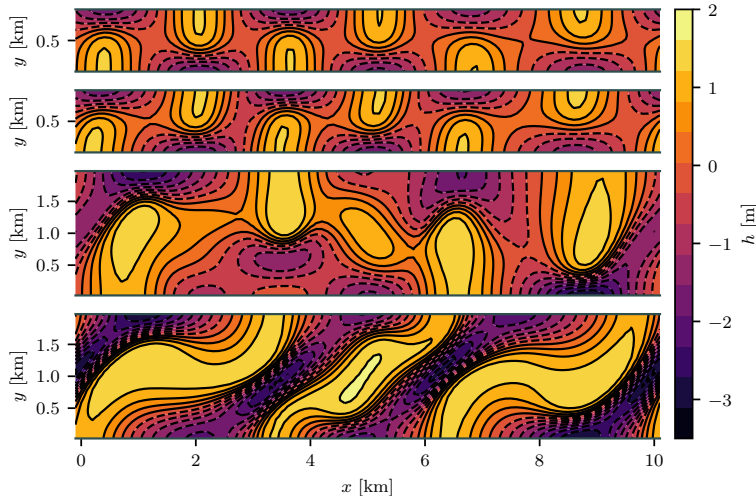


Figure 5.8: As Figure 5.7 but after $t = 30$ years. From top to bottom panel: $(B, \varphi) = (1 \text{ km}, 0^\circ)$, $(1 \text{ km}, 50^\circ)$, $(2 \text{ km}, 0^\circ)$ and $(2 \text{ km}, 50^\circ)$.

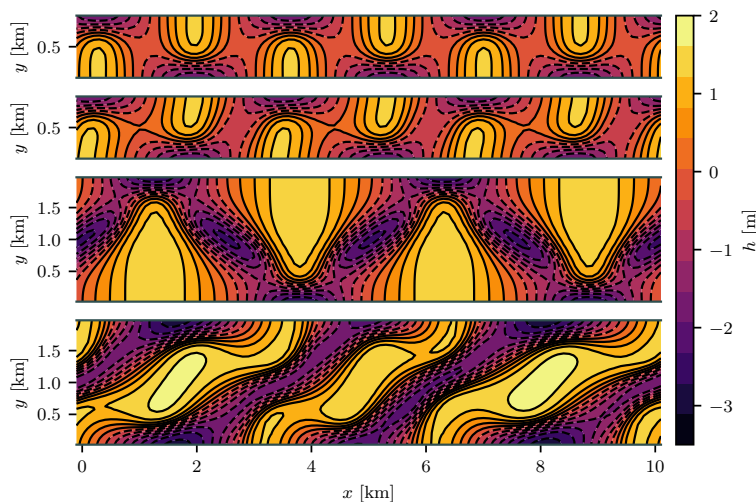


Figure 5.9: As Figure 5.7 but after $t = 150$ years. From top to bottom panel: $(B, \varphi) = (1 \text{ km}, 0^\circ)$, $(1 \text{ km}, 50^\circ)$, $(2 \text{ km}, 0^\circ)$ and $(2 \text{ km}, 50^\circ)$.

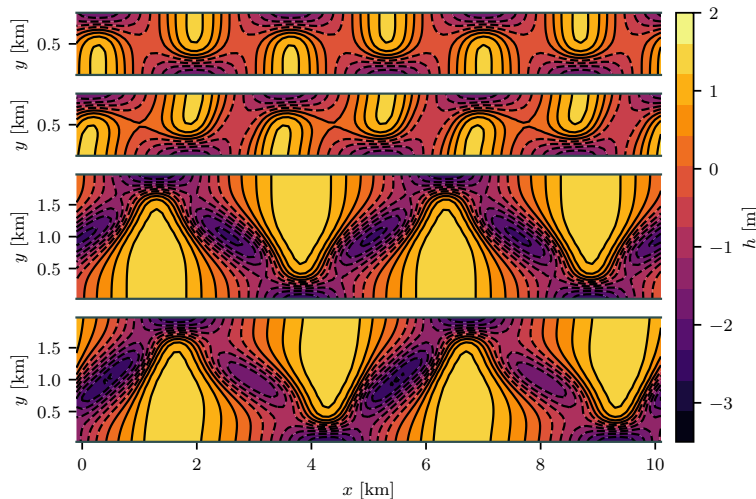


Figure 5.10: As Figure 5.7 but after $t = 325$ years. From top to bottom panel: $(B, \varphi) = (1 \text{ km}, 0^\circ)$, $(1 \text{ km}, 50^\circ)$, $(2 \text{ km}, 0^\circ)$ and $(2 \text{ km}, 50^\circ)$.

Figure 5.7–5.10 show snapshots of the bottom patterns of the four simulations at four different moments in time: $t = 10, 30, 150$ and 325 yr. After 10 years (Figure 5.7), the patterns resemble the patterns of the eigenvectors of the Jacobian at the flat bottom corresponding to the largest eigenvalue (see Chapter 4). When the Coriolis effect is neglected ($\phi = 0^\circ$), in the narrow channels ($B = 1$ km), an alternating bar pattern forms, while in the wider channels ($B = 2$ km), a braided pattern with one bar/trough in the middle forms. As suggested by the results of Chapter 4, in the simulations where the Coriolis effect is included ($\phi = 50^\circ$ N), the pattern is a combination of bars and oblique ridges which are rotated anticlockwise with respect to the main channel axis. The ridges are more pronounced in the wider channel.

After 30 years (Figure 5.8), the narrow channels are close to equilibrium (see Figure 5.6). The wider channels are still in their transient phase. During that phase, the bars in the middle connect to those at the sides. In the simulation with the Coriolis effect included, the bars on the right and left side of the channel are connected, thereby forming meandering ridges.

After 150 years (Figure 5.9), all patterns seem to be stationary (see Figure 5.6). In the first simulations ($B = 1$ km, $\varphi = 0^\circ$), a pattern forms with bars extends over the middle axis of the channel. In the second simulation ($B = 1$ km, $\varphi = 50^\circ$ N), the pattern is fairly similar to that in the first simulation, but the Coriolis effect skews the pattern slightly. The latter results in the formation of a shallow sill between the alternating bars on one side and a deeper channel on the other side of the bars. In the third simulation ($B = 2$ km, $\varphi = 0^\circ$), the bars in the middle fully merged with those on the side. Compared to the first simulation, the bars are wider at the closed boundaries and form somewhat triangular bars opposed to the thin finger shaped bars in the narrow channels. In the fourth simulation ($B = 2$ km, $\varphi = 50^\circ$ N) the pattern remains in the shape of meandering ridges. They are not completely static, but their evolution is very slow. This period of slow evolution is followed by a quick adjustment after 2.5 centuries (see Figure 5.6). At that time, the ridges break into separate bars and form a pattern similar to the pattern observed in the third simulation in which the Coriolis effect is neglected. The main difference is that in the fourth simulation the pattern is slightly skewed (Figure 5.10).

Figure 5.11 shows the amplitudes of the Fourier coefficients $h_{m,n}$ versus time. The colored lines are the four coefficients with the largest amplitude after 500 years. Their along-channel and lateral wavenumbers are shown in the top panel of the figure. The gray lines are the amplitudes of the remaining coefficients. The figure reveals that in the narrow channel ($B = 1$ km) the Fourier mode that initially grows the fastest (red line) remains dominant over time. However, in the wider channel this is not the case. Moreover, the bottom panels show the initial difference and eventual similarity between the Fourier spectrum of the 2 km wide channel with and without the Coriolis effect taken into account.

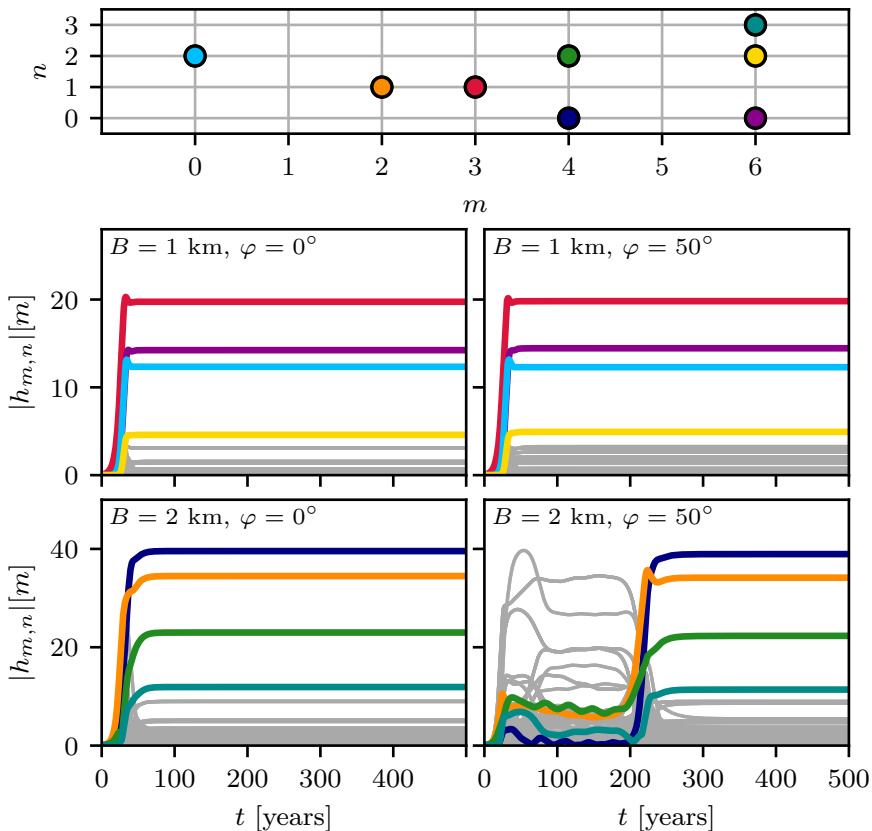


Figure 5.11: Bottom four panels: amplitude of Fourier coefficient $h_{m,n}$ versus time t for the four simulations. The four Fourier modes that have the largest amplitude after 500 years are colored. The corresponding modenumbers m and n are shown in the top panel. Parameter values used are as in Table 5.1.

5.3.3 Continuation

The top panel of Figure 5.12 shows the root-mean square height h_{rms} of morphodynamic equilibria as a function of channel width B . The white dots are unstable equilibria and the gray dots are stable ones. For this parameter setting, the critical channel width at which the flat bottom loses its stability is between $B = 0.8$ and $B = 0.85$ km. The bottom panels of Figure 5.12 show the morphodynamic equilibria for channel widths of $B = 0.5, 0.85, 1, 1.5$ and 1.8 km (indicated by the stars in the top panel of the figure). The first morphodynamic equilibrium is a flat bottom, which is linearly stable for these parameter values. For $B = 0.85$ km, the equilibrium bathymetry is nontrivial, with the bars slightly extending over the mid-channel axis. For wider channels, the bars are further extended over the channel axes. Moreover, whereas the bars attain their maximum height on the side of the channel for $B = 0.85$ and $B = 1$ km, the location of maximum bottom height is detached from the channel boundary for larger channel widths. The second panel in Figure 5.12 shows the amplitudes of the Fourier coefficients $|h_{m,n}|$ (> 0.25 m) as a function of channel width B . The colors correspond to those in Figure 5.11. The four Fourier modes with the largest amplitude after 500 years in the first time integration run ($B = 1$ km and $\varphi = 0^\circ$, see Figure 5.11) are the same as the ones that form the morphodynamic equilibria for $850 \leq B \leq 1800$ m. Furthermore, Figure 5.12 reveals that the number of relevant Fourier modes increases for increasing channel width.

5.4 Discussion

5.4.1 Results of LSA of flat bottom as indicators for long-term behavior

The linear stability analyses (LSA) (Seminara and Tubino, 2001, Schramkowski et al., 2002, Chapters 3 and 4) have provided fundamental knowledge about the mechanisms that explain the initial formation of tidal bars as perturbations of a flat bed. The time evolutions in the previous section allow us to assess the predictive capability of long-term tidal bar patterns by the LSA of the flat bottom. When we compare the pattern that initial forms and the final patterns in the time integration simulations, we observe that in the narrow (1 km wide) channels the wavelength and number of bars in the lateral direction do not change over time. That is, the Fourier mode that initially grows the fastest remains the dominant one in the spectrum in the long-term. So in these cases, the fastest growing pattern from the LSA resembles the final pattern of the time integration reasonably well, although the other Fourier modes are not negligible. However, in the wider channels (2 km), the dominant tidal bar wavelength in the initial formation (Figure 5.7) is smaller than that in the final

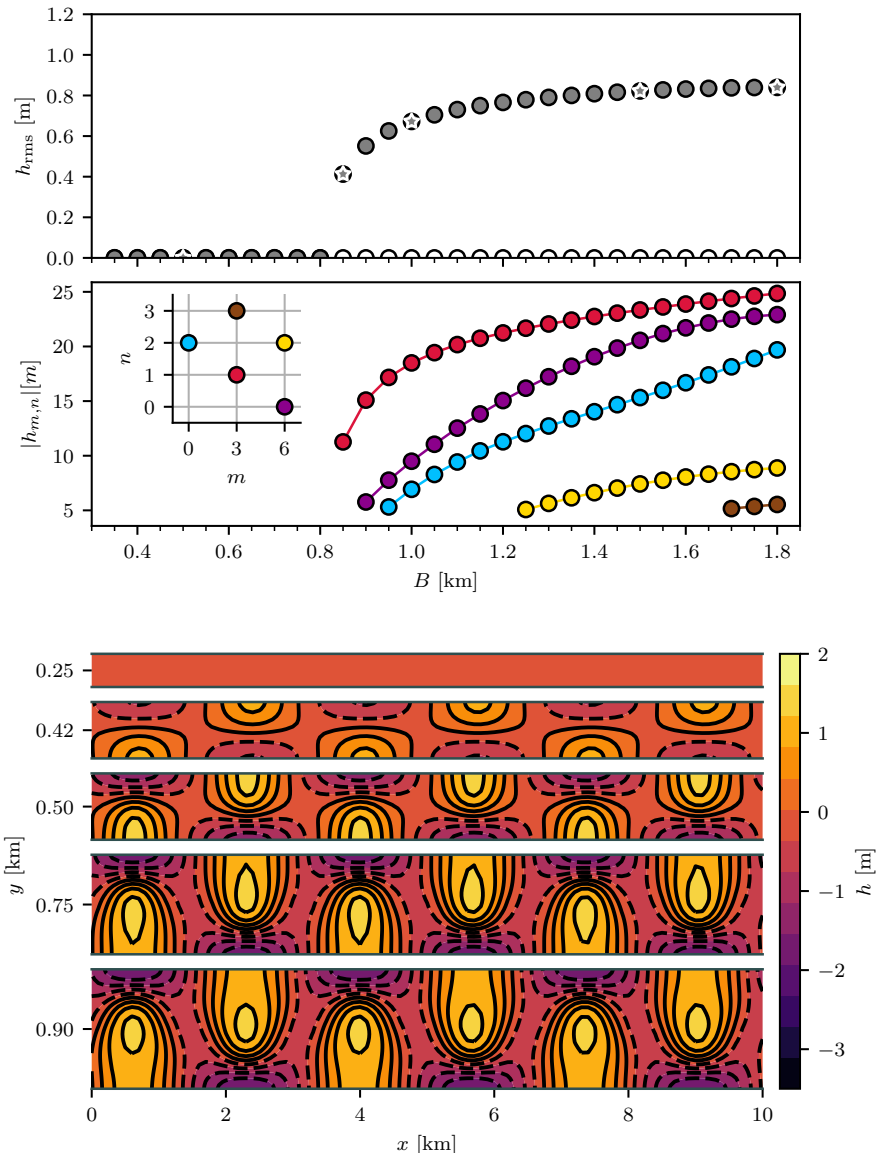


Figure 5.12: Top panel: root-mean square height h_{rms} of morphodynamic equilibria versus channel width B . The gray dots denote stable equilibria, while the white dots represent unstable ones. The patterns corresponding to the dots with a white star are shown in the bottom panels: $B = 0.5, 0.85, 1, 1.5, 1.8$ km. The middle panel shows the amplitudes of the Fourier coefficients of the nontrivial patterns for $B \geq 850$ m. The parameter values used are $u_c = 0$, $u_w = 0$, $\varphi = 0^\circ$, $c_t = 0$ and the depth $H - h + \zeta$ in c_b is replaced by the undisturbed depth H . Other parameter values are as in Table 5.1.

pattern (Figure 5.10). Furthermore, the bottom has a braided pattern during the initial formation, while in the final pattern bars have merged to form an alternating tidal bar pattern. The difference between the long-term bottom patterns and the fastest growing pattern following from the LSA studies is the largest in the simulation with $B = 2$ km and $\varphi = 50^\circ$ N. Here, the oblique tidal sand ridges that initially form hardly resemble the final bed forms that show an alternating pattern.

5.4.2 Comparison with field observations and numerical studies

Van Veen (1950) described bottom patterns in tidal channels with ebb and flood channels around the bars (see also van den Berg et al., 1996). In the ebb channels the maximum ebb current is stronger than the maximum flood current and vice versa. Such channels were also identified in the numerical results of Hibma et al. (2003). However, the current study seems to lack the mechanism responsible for the formation of such channels. Figure 5.13 shows the locations where the along-channel current is ebb- or flood-dominant at the end of the time integration (after 1000 years). That is, where $|\max_t(u)| - |\min_t(u)|$ is positive (warmer colors) or negative (colder colors). Furthermore, it shows the pattern of the residual currents (arrows). The figure reveals that on the negative x -side of the bar the current is flood dominant (red), while at the positive x -side it is ebb dominant (blue). So, rather than having ebb or flood dominated channels, the channels are divided in a flood and ebb dominant part. Even though the ebb and flood channels are not present, the structure of the residual current is in agreement with the schematic diagram of estuarine meanders in Ahnert (1960) (Figure 3 in the latter study and Figure 5b of Hibma et al., 2003). In this diagram only at some locations there is a submerged bar between the ebb and flood current trajectories. They attribute the occurrence of the ebb and flood channels to the phase difference between the free surface elevation and the current velocity. In particular, at the locations where the ebb and flood channels occur, there is an overlap in water levels present at high ebb and flood currents (see Figures 6 in both Ahnert (1960) and Hibma et al. (2003)). Due to the local nature (with the rigid-lid assumption) of the current model, this overlap is always there. However, to study the effect of variations in the phase difference between the currents and the free surface elevation, a global model is needed.

The tidal bars simulated in the laboratory by Leuven and Kleinhans (2019) and those observed in the Exe estuary (Figure 1.1), extend over the middle axis of the channel. This corresponds to the results above. Moreover, the laboratory bars in Leuven and Kleinhans (2019) resemble the triangular shape of the bars obtained with our model in 2 km wide channels (Figure 5.10). However, in the laboratory they do not seem to form by merging two bars on the side and one in the middle of the channel, as observed in the result of the time integration with

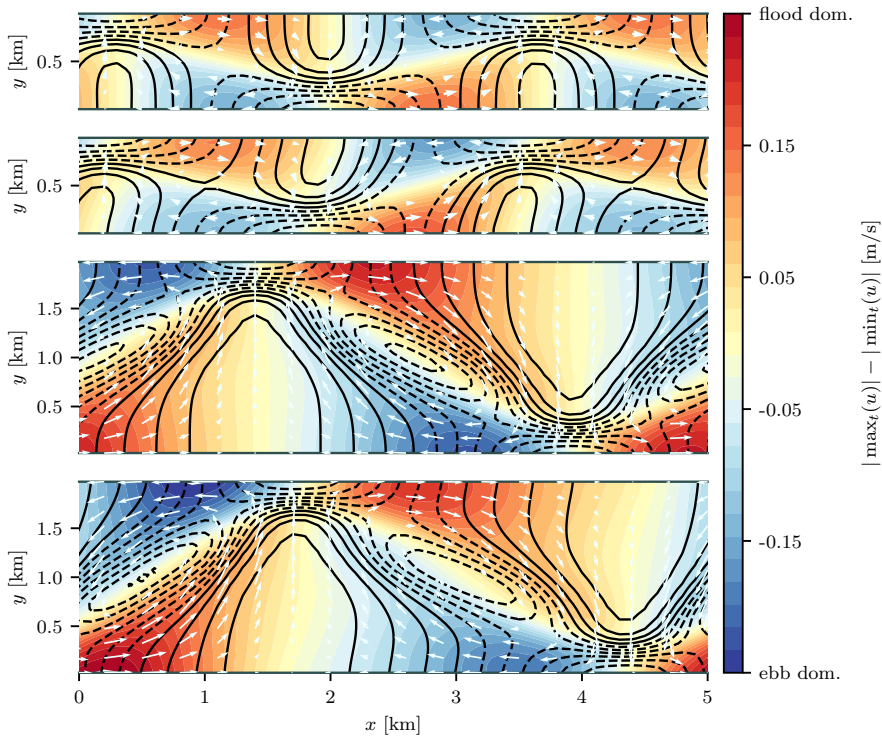


Figure 5.13: Black contour lines denote the bottom height as in Figure 5.9, but for only $0 \leq x \leq 5$ km. Dashed lines denote a negative bottom height, while solid lines denote a positive bottom height. The colors denote the (absolute) maximum value of the along-channel current velocity minus the absolute value of its minimum over a tidal cycle. Red colors denote stronger maximum flood currents, while blue colors denote stronger maximum ebb currents. The white arrows depict the spatial distribution of the residual current.

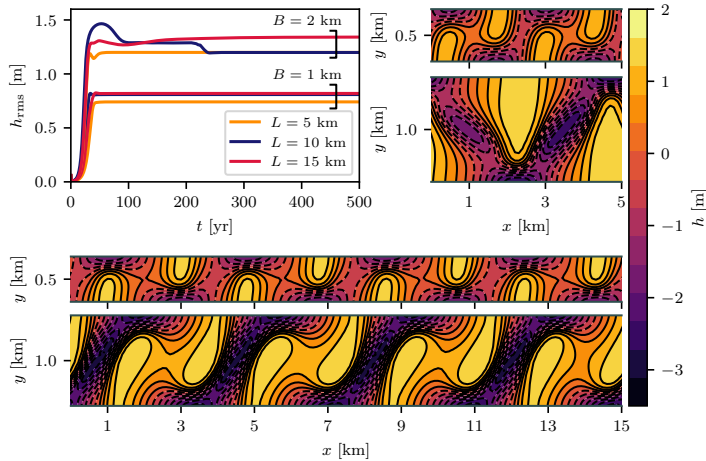


Figure 5.14: Root-mean square height h_{rms} versus time t for different channel widths B and domain lengths L (top left panel). The dark blue curves ($L = 10 \text{ km}$) correspond with those (cyan and red) in Figure 5.6. The top right and bottom panels show the bottom pattern after 500 years for domain lengths of $L = 5 \text{ km}$ and $L = 15 \text{ km}$, respectively. Parameters are as in Table 5.1.

$B = 2 \text{ km}$ and $\varphi = 0^\circ$. Moreover, the sills connecting the bars, as observed in the laboratory, are not reproduced in the current numerical simulations. Only when the Coriolis effect was taken into account sills formed, but only on one side of the bars.

In the four time integration simulations, the value of the Coriolis parameter seems to be mostly affecting the transient behavior and to a much lesser extent the equilibrium patterns. This is in good correspondence with the fact that the bathymetries both in the numerical studies of, on one hand van der Wegen and Roelvink (2012), who ignore Coriolis, and on the other hand Dam et al. (2016) and Nnafie et al. (2018), who include Coriolis, reproduced the observed bottom topography in the Western Scheldt reasonably well. No clear signature of the Coriolis effect was observed.

5.4.3 Model limitations

The first important limitation of the model in this study is that it does not allow for intertidal areas, while natural tidal bars often are only submerge during a part of the tidal cycle. The second limitation is that the contribution of the free surface elevation due to the external pressure gradient on the water depth is in many systems significant, whereas in this model only the free surface elevation as a result of the bottom height is considered. These two choices are

numerically rather than physically motivated and therefore deserve additional attention. A third limitation is the dependency of the model results on the choice of the domain length L . When L is too long, the assumption of along-channel uniformity is violated. However, when the domain length L is too short, the number of along-channel Fourier modes is strongly restricted thereby limiting the dynamics. Figure 5.14 shows the root-mean square height and the bottom pattern after 500 years for a channel domain of $L = 5$ and $L = 15$ km ($\pm 50\%$ of the default channel length). The channels are 1 and 2 km wide and the latitude $\varphi = 50^\circ$ N. The comparison of the result in Figure 5.10 with those in Figure 5.14 reveals that the results in a 5, 10 or 15 km long channel agree quantitatively with those obtained in the 1 km wide channel. Quantitatively, the root-mean square height and the along-channel wavelength are slightly different. In the 2 km wide channel, the results show a stronger sensitivity to the choice of channel length. When the channel length is halved ($L = 5$ km), the time interval in which the root-mean square height temporary stopped changing, as in the simulation with $L = 10$ km (between 100 and 200 years), is not present anymore. When the channel length is increased by 50% ($L = 15$ km), the rapid adjustment, as observed around 250 years in the simulation of $L = 10$ km, is not found in the first 500 years of simulation. In fact, the pattern after 500 years in the long channel (15 km) resembles that of the original simulation ($L = 10$ km) after 150 years (bottom panel Figure 5.9). It is unclear whether this pattern will eventually also change to a pattern similar

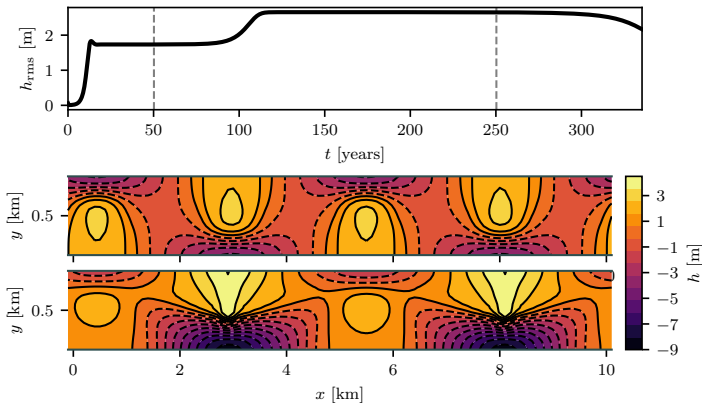


Figure 5.15: Top panel shows the root-mean square height h_{rms} versus time t . The bottom panels show the bottom height versus space after 50 and 250 years, corresponding to the vertical gray lines in the top panel. The solid black line in Figure 5.15 corresponds with the black line in the top panel. The simplified model, as described in the validation section of 5.2.6, is used with parameters values as in Table 5.1 with $B = 1000$ m, $U = 1$ m/s, $H = 5$ m, $u_c = 0$, $u_w = 0$, $\mu = 1 \text{ m}^2 \text{s}^{-1}$ and $\varphi = 0^\circ$.

to the one in the $L = 10$ km simulation (bottom panel in Figure 5.10) if the simulation time would be increased.

A further systematic sensitivity analysis to model parameters is needed before robust conclusions can be made about timescales at which patterns settle in a morphodynamical equilibrium and their associated final heights. Figure 5.15 reveals that in different regions of the parameter space, the dynamics can be vastly different. The top panel shows the time evolution of the root-mean square height of the bottom for the simulation used in Figure 5.5 (i.e., the simplified model as described in the verification section in 5.2.6). The bottom panels show the patterns after 50 and 250 years. As in the simulation with $B = 2$ km and $\varphi = 50^\circ$, the bottom height is almost constant after an initial adjustment (in this case after a few decades), but then (after a few centuries) changes drastically again. After 350 years the model crashed (likely due to a numerical instability). The pattern after 250 years is characterized by an asymmetric distribution of sediments with respect to the channel axis; most sediments are deposited on left side of the channel (viewed in the positive x -direction). This is another example where the system seems to have found an equilibrium (twice), but then quickly evolves after some time. Other possible extensions of the model are to consider multiple tidal constituents in the tidal forcing and to include the role of river runoff, wind waves, vegetation, sand-mud mixtures and stratification on the hydro- and morphodynamics.

5.5 Conclusions

The long-term dynamics of tidal bars in a confined tidal channel is studied with a numerical model of intermediate complexity. Its formulation allows a comparison of the bottom evolution with that predicted by linear stability analyses of a flat bottom. The evolution of the bathymetry starting from a randomly perturbed flat bottom is simulated over a few centuries for tidal channels of different widths and at different latitudes. Eventually, in all simulations the tidal bars stopped evolving after a certain amount of time. Also, in all simulations the tidal bars extended over the middle axis of the channel; a characteristic also observed in nature and in the laboratory. The differences between the simulations yields a first insight in the sensitivity of the tidal bar dynamics to channel width and the Coriolis effect. In the 1 km wide channels, the initially forming patterns are only slightly adjusted over time (by extending over the middle axis). The Coriolis effect only slightly skews this pattern, thereby forming shallow sills between the bars. In the 2 km wide channels the dynamics is richer. The initially braiding pattern evolves in an alternating bar pattern by merging tidal bars in the middle of the channel with those on the side, thereby also increasing the tidal bar wavelength. Moreover, in the 2 km wide channel located at a latitude of 50° N, the bars seem to reach a morphodynamic equilibrium after a century, but rapidly change, after approximately 2.5 centuries,

into a drastically different pattern. The pattern observed after a century is very different from the pattern in the 2 km wide channel when the Coriolis effect was neglected. However, the pattern after 2.5 centuries is, like the one observed in the 1 km wide channel merely a skewed version of the case with the channel located at latitude 0° . This highlights one of the the difficulties of studying equilibrium tidal bar patterns by means of a time integration; it is unclear when and if a pattern is in morphodynamic equilibrium. A numerical continuation shows the morphodynamic equilibria for different channel widths. For increasing widths, the bars extend further over the channel axes and the maximum bottom height of the patterns moves away from the channel boundary.